Research Article

Light yield and thermal quenching of Ce^{3+} and Pr^{3+} co-doped $LaBr_3$:Sm^{2+} near-infrared scintillators

Casper van Aarle [a,*], Nils Roturier [a], Daniel A. Biner [b], Karl W. Krämer [b], Pieter Dorenbos [a]

[a] *Faculty of Applied Sciences, Delft University of Technology, Mekelweg 15, Delft, The Netherlands*
[b] *Department of Chemistry and Biochemistry, University of Bern, Freiestrasse 3, Bern, Switzerland*

ARTICLE INFO

ABSTRACT

$LaBr_3$:Ce^{3+} is a compound with excellent scintillation properties, but its ultraviolet emission does not match well with the detection efficiency curves of silicon based photodetectors. In this work, Sm^{2+} is studied as an activator for $LaBr_3$ as its near-infrared emission can be detected with close to 100% efficiency by such photodetectors. $LaBr_3$:Sm^{2+} single crystals were grown with and without co-doping of Ce^{3+} or Pr^{3+}. The samples were studied by means of X-ray excited and photoluminescence spectroscopy at temperatures between 10 K and 300 K. Their spectroscopic properties are compared to $LaBr_3$:Ce^{3+} and $LaBr_3$:Eu^{2+}. The effect of using Ce^{3+} or Pr^{3+} as scintillation sensitiser for Sm^{2+} is assessed. It is found that energy transfer from host to Sm^{2+} greatly improves upon Ce^{3+} co-doping, but the quenching temperature of the Sm^{2+} emission decreases. The quenching mechanism of both the Ce^{3+} and Sm^{2+} emission in $LaBr_3$ is elaborated on. Furthermore, the effect of charge compensating defects on the light yield and spectroscopic properties is discussed.

1. Introduction

When $LaBr_3$:Ce^{3+} was first discovered as a γ-ray scintillator in 2001, it was found to have a light yield of 61,000 ph/MeV and an energy resolution of 2.8% at 662 keV was attained [1]. Its high light yield and fast decay time of 30 ns make $LaBr_3$:Ce^{3+} suitable for medical imaging applications where high time resolution and count rates are required, such as time-of-flight positron emission tomography [2] and photon-counting computed tomography [3]. Its energy resolution makes it possible to discriminate between γ-rays with smaller energy difference than what is achieved with more commonly used NaI:Tl⁺ scintillators. $LaBr_3$:Ce^{3+} is therefore also suitable for use in γ-ray spectrometers [4] and radio-isotope identification devices [5]. These days, $LaBr_3$:Ce^{3+} scintillation crystals are widely available as commercial products.

Another useful property of $LaBr_3$:Ce^{3+} is its exceptionally large Stokes shift of 0.54 eV [6] resulting in low self-absorption losses [7], which is favourable for applications where large crystals are required. Even in large crystals of $CeBr_3$ self-absorption losses are minimal [7,8]. The reason behind this large Stokes shift has been studied by Andriessen et al. [9]. $LaBr_3$ has the UCl_3 type crystal structure, the same as $CeBr_3$ and $PrBr_3$, in which the cation has 9 fold coordination. Upon further decrease of the cation size, e.g. $NdBr_3$, compounds start to crystallise in the $PuBr_3$ type structure, where the cation has 8 fold coordination [10]. Ab initio calculations have shown that upon 4f → 5d excitation of Ce^{3+}, the corresponding decrease in its ionic radius causes deformation of the direct environment of Ce^{3+}. One bromide ion is pushed away and the other 8 are pulled towards Ce^{3+}, effectively reducing the coordination number to 8 [9]. This increases the crystal field splitting and moves the lowest 5d excited state to even lower energy without the usual broadening of the Ce^{3+} emission bands, decreasing the overlap between the Ce^{3+} emission and its absorption bands.

In 2013, significant improvements were made to $LaBr_3$:Ce^{3+} by means of Sr^{2+} co-doping. The co-doping greatly improved the scintillator's proportionality and resulted in a slight increase in light yield to 78,000 ph/MeV. When coupled to a Hamamatsu R6231-100 photomultiplier tube (PMT), the attained energy resolution of 2.04% was close to the fundamental limit achievable when 24,000 scintillation photons are being detected [11]. Further improvement of the energy resolution thus requires increasing the number of detected photons.

The number of detected photons is determined by the light yield of a scintillator and the detector efficiency. Only 31% of the scintillation photons were detected when recording the 2.04% energy resolution pulse height spectrum [11]. Silicon based photodetectors, such as avalanche photodiodes (APD) or silicon photomultipliers (SiPM) typically have much higher detection efficiencies which can reach close to 100% in the visible and NIR part of the spectrum. For wavelengths shorter than 400 nm, the detection efficiency of such photodetectors is typically lower due to a rapid increase in the absorption coefficient of

---
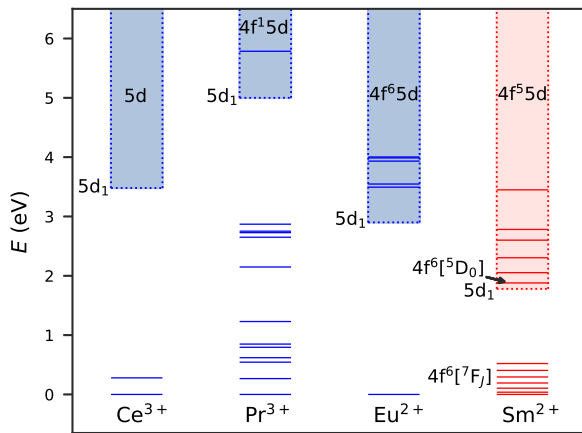
Fig. 1. Diagram showing the energy levels of Ce^{3+}, Pr^{3+}, Eu^{2+}, and Sm^{2+} in $LaBr_3$. The horizontal lines represent $4f^n$ levels. The ranges of the $4f^{n-1}5d$ levels are shown by coloured bands.

silicon, causing scintillation photons to be absorbed in the dead layer of the detector. In the case of $LaBr_3:Ce^{3+},Sr^{2+}$, this reduces the number of detected photons by approximately 20% [12]. A solution to this problem would be the use of activators that emit at wavelengths longer than 400 nm.

Some activators other than Ce^{3+} have already been attempted for $LaBr_3$, among which are Pr^{3+} and Eu^{2+}. $LaBr_3:Pr^{3+}$ shows exclusively Pr^{3+} $4f^2 \to 4f^2$ line emission with a decay time of 11 μs. An energy resolution of 3.2% and light yield of over 60,000 ph/MeV have been observed when coupled to an APD [13]. $LaBr_3:Eu^{2+}$ shows Eu^{2+} $4f^65d \to 4f^7$ broad band emission around 430 nm. A light yield of 43,000 ph/MeV and energy resolution of 6% have been reported [14].

Sm^{2+} is another potential candidate as an activator for $LaBr_3$. Its energy levels are shown in Fig. 1 together with those of Ce^{3+}, Pr^{3+}, and Eu^{2+}. The energy of the lowest $4f^{n-1}5d$ levels ($5d_1$) of Ce^{3+} and Eu^{2+} are based on their $4f^{n-1}5d \to 4f^n$ emission wavelengths in $LaBr_3$ [6]. The energy of the $5d_1$ levels of Pr^{3+} and Sm^{2+} are calculated using their constant energy difference to Ce^{3+} and Eu^{2+}, respectively [15,16].

At room temperature, Sm^{2+} shows exclusively $4f^6[^5D_0] \to 4f^6[^7F_J]$ line emission when the $5d_1$ level lies more than about 0.2 eV above the $4f^6[^5D_0]$ level. When the $5d_1$ level lies below the $4f^6[^5D_0]$ level, exclusively $4f^55d \to 4f^6$ broad band emission is observed. In compounds where the $5d_1$ level lies less than 0.2 eV above the $4f^6[^5D_0]$ level, the $4f^6 \to 4f^6$ and $4f^55d \to 4f^6$ emissions are often observed simultaneously. The ratio between the $4f^6 \to 4f^6$ and $4f^55d \to 4f^6$ emission is temperature dependent. With increasing temperature, the $4f^6 \to 4f^6$ emission lines decrease in intensity and $4f^55d \to 4f^6$ emission intensity increases. In compounds where Sm^{2+} shows exclusively $4f^55d \to 4f^6$ emission at room temperature, $4f^6 \to 4f^6$ line emission is often still observed at cryogenic temperatures. For any given temperature, the intensity of these $4f^6 \to 4f^6$ emission lines decreases with decrease of the $5d_1$ level energy.

The Sm^{2+} $4f^55d \to 4f^6$ emission typically lies in the near-infrared part of the spectrum and can therefore be efficiently detected by silicon based photodetectors. Its decay time lies between 1.5 μs and 15 μs [17,18], which is fast enough for application in low count rate γ-ray spectroscopy. Compounds with exclusively Sm^{2+}-doping have been reported to show light yields of up to 33,000 ph/MeV [19]. A benefit to using Sm^{2+} is that $4f^55d \to 4f^6$ emission may have any of the ^7F_J levels as final state, while absorption exclusively takes place from the $^7F_0$ ground state. As a consequence, self-absorption losses in Sm^{2+}-doped scintillators are minimal, especially if the Sm^{2+} concentration can remain low [20].

Radiationless energy transfer is possible when the emission bands of a sensitiser overlap with the absorption bands of an acceptor [21].

Since the Sm^{2+} $4f^55d \to 4f^6$ emission lies in the infrared, its $4f^6 \to 4f^55d$ absorption bands cover the entire visible spectrum. This makes it possible to sensitise Sm^{2+} with many different co-dopants. Efficient sensitisation of Sm^{2+} by Eu^{2+} for scintillation was first demonstrated in $SrI_2:Eu^{2+},Sm^{2+}$, where it was found that almost all Eu^{2+} excitations are transferred non-radiatively to Sm^{2+} upon co-doping with as little as 0.5% Sm^{2+} [18]. The same strategy has yielded an energy resolution of 3.2% and light yield of 45,000 ph/MeV when coupling a $CsBa_2I_5:2\%Eu^{2+},\%Sm^{2+}$ crystal to an APD [22].

In this work the feasibility of using Sm^{2+} as a dopant in $LaBr_3$ is assessed. Additionally, the effect of using Ce^{3+} or Pr^{3+} as a scintillation sensitiser is explored. A comparison is made with the spectroscopic and scintillation properties of $LaBr_3:Eu^{2+}$. For this study, $LaBr_3$ samples were synthesised with a 1% doping concentration of Sm^{2+} or Eu^{2+}. Two Sm^{2+}-doped samples were co-doped with 5% Ce^{3+} or 1% Pr^{3+}. Additionally, $CeBr_3:1\%Sm$ is studied. The scintillation characteristics are assessed through X-ray excited emission spectra. Thermoluminescence (TL) measurements are performed to study the effect of charge compensating defects. Lastly, photoluminescence measurements are performed to study the energy transfer from host and sensitiser to Sm^{2+} and to determine the location of the Sm^{2+} $5d_1$ level.

2. Experimental techniques

Crystals of $LaBr_3$ and $CeBr_3$ doped with Ce^{3+}, Pr^{3+}, Sm^{2+}, and/or Eu^{2+} were grown from the binary halides MBr_3 (M = La, Ce, Pr) and MBr_2 (M = Sm, Eu) by the vertical Bridgman technique. The binary halides MBr_3 (M = La, Ce, Pr, Sm, Eu) were prepared by the ammonium bromide method [23]. The rare earth oxide (La_2O_3, 5N; CeO_2, 5N; Pr_6O_{11}, 5N5; Eu_2O_3, 5N, all from Metall Rare earth Ltd.; Sm_2O_3, > 3N, Fluka) was dissolved in concentrated HBr acid (47%, suprapur, Merck) and an excess of NH_4Br (p.a., sublimed, Merck) added in a M to NH_4 ratio of 2 to 7. The solution was dried up on a sand bath to yield the anhydrous ternary compound $(NH_4)_3MBr_6$, which is subsequently decomposed to MBr_3 by heating in vacuum. $LaBr_3$, $CeBr_3$, $PrBr_3$, and $SmBr_3$ were sublimed in a silica apparatus under high vacuum for purification. $EuBr_2$ was obtained by heating $EuBr_3$ in vacuum at 500 °C and used without further purification. $SmBr_2$ was obtained by reduction of $SmBr_3$ with Sm metal (3N; Alfa) in a Ta ampoule. The Ta ampoule was sealed by helium arc-welding and enclosed into a silica ampoule under vacuum. The ampoule was heated to 900 °C for 7 days.

Stoichiometric amounts of the binary halides (about 5 g per sample) were sealed in Ta ampoules. An inert ampoule, such as Ta, is required to maintain a pure Sm^{2+} state in the crystal. $LaBr_3:1\%$ Eu^{2+} was grown in a silica ampoule, since Eu^{2+} is less sensitive to oxidation than Sm^{2+}. The ampoules were heated in a Bridgman furnace to 800 °C ($LaBr_3$) or 750 °C ($CeBr_3$), respectively, i.e., above the congruent melting point of the host material. After 1 day at constant temperature, the crystal growth was started by slowly moving up the furnace. The samples were cooled to room temperature within about 10 days. Crystals were cleaved from the boules for spectroscopic investigations. The denoted doping level represents the melt composition. Since starting materials and products are highly hygroscopic and sensitive to oxidation, all handling was done under strictly dry and oxygen-free conditions (H_2O and $O_2 < 0.1$ ppm) in glove boxes and sealed sample containers. Experiments on $LaBr_3$ and $CeBr_3$ without divalent dopants were performed on samples of which the synthesis was previously reported in literature: $LaBr_3:5\%Ce^{3+}$ [24], $LaBr_3:0.5\%Pr^{3+}$ [6], and $CeBr_3$ [25].

X-ray excited emission spectra were recorded using a Varex VF-80JM X-ray tube with tungsten anode operated at 80 kV and 1 mA. A 1 mm thick copper filter was used to filter out the low energy X-rays that otherwise may cause radiation damage to the sample. The samples were mounted directly on the cold finger of a Janis He or N_2 cryostat and placed in front of the X-ray tube. The sample chamber was kept at a pressure below 10^{-4} mbar during operation. The sample emission was monitored under a 90° angle with respect to the X-ray beam and
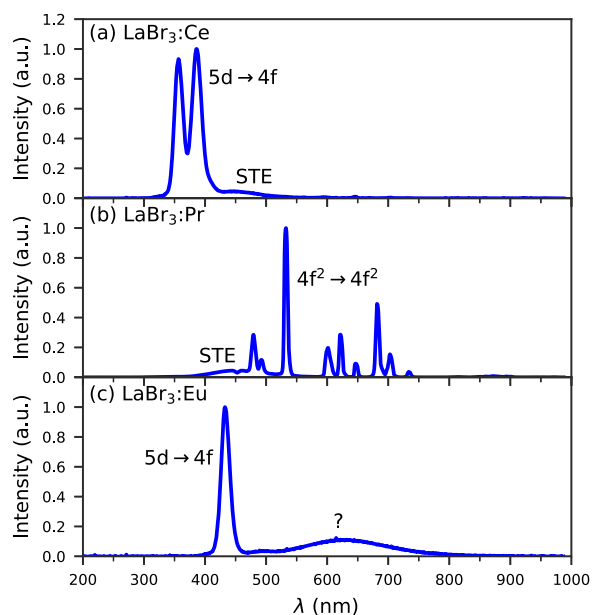
Fig. 2. X-ray excited emission spectra of (a) LaBr$_3$:5%Ce^{3+}, (b) LaBr$_3$:0.5%Pr^{3+}, and (c) LaBr$_3$:1%Eu^{2+} at 10 K.

controlled in an identical way as for the photoluminescence excitation and emission spectra. The excitation light was filtered out using an optical filter, after which the emission light passed through a SpectraPro-SP2358 monochromator before being detected by a Hamamatsu R7600U-20 PMT. The signal from the PMT was converted to a digital signal using a CAEN DT5730 digitizer.

3. Results

As the effect of co-doping LaBr$_3$:Sm^{2+} with Ce^{3+} and Pr^{3+} is studied, spectroscopic results on LaBr$_3$:5%Ce^{3+} and LaBr$_3$:0.5%Pr^{3+} are also presented to yield information on the role of these dopants in the scintillation mechanism. Fig. 2a shows the X-ray excited emission spectrum of LaBr$_3$:5%Ce^{3+}. The two strong emission bands around 380 nm are ascribed to the Ce^{3+} 5d → 4f transitions. The weak band around 440 nm was previously assigned to self-trapped exciton (STE) emission of LaBr$_3$ [6].

The emission spectrum of LaBr$_3$:0.5%Pr^{3+} is shown in Fig. 2b. The spectrum contains predominantly sharp emission lines that are ascribed to the Pr^{3+} 4f^2 → 4f^2 transitions. It shows a weak broad band around 440 nm, similar to the STE emission observed in LaBr$_3$:Ce^{3+}.

LaBr$_3$:1%Eu^{2+} is studied for comparison with LaBr$_3$:Sm^{2+}, as Eu^{2+} has the same valence and similar ionic radius as Sm^{2+} and is spectroscopically more simple. Fig. 2c shows the X-ray excited emission spectrum of LaBr$_3$:1%Eu^{2+}. It shows an intense emission band with a maximum at 430 nm, which is assigned to the 4f^{6}5d → 4f^7 transition [6]. Additionally, a broad emission band of unknown origin is observed between 500 nm and 800 nm.

Fig. 3a shows the X-ray excited emission spectra of LaBr$_3$:1%Sm^{2+}. At 10 K it shows almost exclusively sharp line emission between 680 nm and 850 nm that corresponds to the 4f^6[^{5}D$_0$] → 4f^6[^{7}F$_J$] transitions of Sm^{2+}. When increasing the temperature to 100 K, a broad band with a maximum at 790 nm appears and the intensity of the line emission decreases. Based on the Eu^{2+} 4f^{6}5d → 4f^7 emission wavelength, the Sm^{2+} 4f^{5}5d → 4f^6 emission wavelength is expected near 750 nm [16]. Therefore, the broad band is assigned to the Sm^{2+} 4f^{5}5d → 4f^6 emission. At 200 K, the 4f^6 → 4f^6 lines have completely disappeared and the 4f^{5}5d → 4f^6 has gained further in intensity. Between 200 K and 300 K, the intensity of the 4f^{5}5d → 4f^6 decreases and at 300 K only 20% of the intensity remains.

Fig. 3b shows the X-ray excited emission spectra of LaBr$_3$:5%Ce^{3+}, 1%Sm^{2+}. The emission spectrum at 10 K again shows Sm^{2+} 4f^6 → 4f^6 line emission, but the 4f^{5}5d → 4f^6 is already visible at this temperature as well. This shows that Ce^{3+} doping slightly lowers the Sm^{2+} 4f^{5}5d energy level with respect to the 4f^6[^{5}D$_0$] level, likely caused by an increase in crystal field splitting strength. In addition to the Sm^{2+} emission, weak Ce^{3+} 5d → 4f emission bands are visible between 350 nm and 420 nm. Again, upon increasing the temperature the Sm^{2+} 4f^6 → 4f^6 emission decreases in intensity while the 4f^{5}5d → 4f^6 emission increases until it quenches between 200 K and 300 K.

The X-ray excited emission spectra for LaBr$_3$:1%Pr^{3+},1%Sm^{2+} are shown in Fig. 3c. At all temperatures, the spectrum contains intense Pr^{3+} 4f^2 → 4f^2 lines in addition to the Sm^{2+} emission, indicating that transfer from Pr^{3+} is inefficient. At 10 K, it can be seen at 825 nm that still a Sm^{2+} 4f^6 → 4f^6 line is visible on top of the 4f^{5}5d → 4f^6 emission, but at higher temperatures this has already disappeared. As opposed to LaBr$_3$:1%Sm^{2+} and LaBr$_3$:5%Ce^{3+},1%Sm^{2+}, the intensity of the Sm^{2+} 4f^{5}5d → 4f^6 emission is highest at 10 K and steadily decreases upon increase of temperature.

In Fig. 3d, the X-ray excited emission spectra of CeBr$_3$:1%Sm^{2+} are shown. Similar to LaBr$_3$:5%Ce^{3+},1%Sm^{2+}, it shows weak Ce^{3+} 5d → 4f emission between 350 nm and 420 nm. The increase in Ce^{3+} concentration compared to LaBr$_3$:5%Ce^{3+},1%Sm^{2+} has lowered the Sm^{2+} 4f^{5}5d level even further and the Sm^{2+} emission around 790 nm now contains exclusively 4f^{5}5d → 4f^6 emission already at 10 K. Upon increase of the

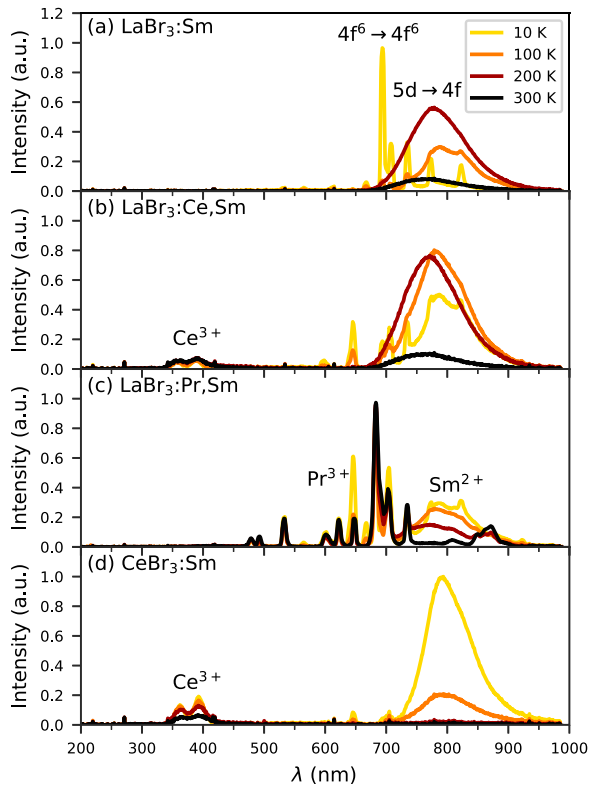was collected through an Ocean Optics QP600-2-VIS optical fibre before being detected using an Ocean Optics QE65Pro spectrometer. Spectra were corrected for the optical fibre attenuation and spectrometer sensitivity. The temperature of the sample was controlled using a Lakeshore temperature controller.

For light yield measurements, a sample holder with fused silica window was filled with small grains of the studied sample. An identical sample holder was filled with small grains of a LaBr$_3$:Ce^{3+} reference sample with known light yield of 76,000 ph/MeV [24]. Light yields were determined by taking the integral of the X-ray excited emission spectrum of the studied sample and comparing it to that of the reference sample at room temperature. The reference sample was mounted on the same cryostat as the studied sample to ensure the geometry of the setup was identical between the measurements.

Thermoluminescence measurements were performed on the same experimental setup as the X-ray excited emission spectra. Samples were given an X-ray dose by irradiating the sample for 10 min at 10 K. After irradiation, the X-ray tube was turned off and a constant heating rate of 15 K/min was applied. The emission spectra were continuously measured by the spectrometer and the integral of the spectra was taken to find the total intensity.

Photoluminescence excitation and emission spectra were measured using a 450 W Xenon lamp and Horiba Gemini 180 monochromator as excitation source. The samples were mounted directly on the cold finger of a Janis He or N$_2$ cryostat and the sample chamber was kept at a pressure below 10^{-4} mbar during the experiment. Emission light from the sample first passed through an optical filter to block the excitation light before passing through a SpectraPro-SP2358 monochromator. For excitation spectra, the emission light was detected using a Hamamatsu R7600U-20 PMT. The excitation spectra were corrected for the intensity of the Xenon lamp. For emission spectra, the emission was detected by a Hamamatsu C9100-13-EM-CCD camera. The temperature was controlled using a Lakeshore temperature controller.

Photoluminescence decay curves were measured using an EKSPLA NT230 OPO laser as excitation source, with a pulse width of 6 ns and repetition rate of 100 Hz. The temperature of the samples was

Fig. 3. X-ray excited emission spectra of (a) LaBr$_3$:1%Sm^{2+}, (b) LaBr$_3$:5%Ce^{3+},1%Sm^{2+}, (c) LaBr$_3$:1%Pr^{3+},1%Sm^{2+}, and (d) CeBr$_3$:1%Sm^{2+}.

Fig. 4. Integrated X-ray excited emission intensities of (a) LaBr$_3$:5%Ce and CeBr$_3$, (b) LaBr$_3$:1%Eu^{2+} and (c) LaBr$_3$:1%Sm^{2+}, LaBr$_3$:5%Ce^{3+},1%Sm^{2+}, LaBr$_3$:1%Pr^{3+},1%Sm^{2+} and CeBr$_3$:1%Sm^{2+}.

temperature, the Sm^{2+} emission rapidly quenches and is already completely gone at 200 K. As opposed to LaBr$_3$:5%Ce^{3+},1%Sm^{2+}, the Ce^{3+} 5d → 4f emission intensity also decreases with increasing temperature, which is ascribed to energy transfer between Ce^{3+} ions increasing the rate of energy transfer to Sm^{2+}.

To further investigate the quenching of Sm^{2+} emission, the integrated emission intensity under X-ray excitation of various compounds is plotted against temperature in Fig. 4. Fig. 4a shows the X-ray excited intensity of Ce^{3+} emission in LaBr$_3$:5%Ce^{3+} and CeBr$_3$. LaBr$_3$:5%Ce^{3+} shows stable emission intensity ranging all the way from 10 K to 600 K. Above 600 K, the intensity drops due to thermal quenching. The value at which the intensity reaching 50% of its maximum values (T_{50}) falls outside the range of the experimental setup. The quenching curve is extrapolated using the single barrier Arrhenius equation and the T_{50} value is estimated to be 715 K.

For CeBr$_3$, the intensity slowly decreases over the entire temperature range, which was also observed by Awater et al. [26] and similar to what was observed for Ce^{3+} emission in CeBr$_3$:Sm^{2+}. In undoped CeBr$_3$, the Ce^{3+} excitations are not lost to Sm^{2+}, but the gradual decrease is ascribed to temperature enhanced concentration quenching. Around 600 K, a steeper decline of the intensity is observed, which is the temperature at which thermal quenching sets in. The value for T_{50} is around 675 K, slightly lower than for LaBr$_3$:5%Ce^{3+}.

Fig. 4b shows the X-ray excited emission intensity of LaBr$_3$:Eu^{2+}. When going from 10 K to 225 K, the emission becomes 4 times more intense, very similar to what was observed in LaBr$_3$:Ce^{3+} co-doped with Ca^{2+}, Sr^{2+} or Ba^{2+}, indicating the formation of electron traps when doping LaBr$_3$ with divalent cations [24]. Further increasing the temperature above 225 K causes the intensity to decrease again due to thermal quenching. The intensity drops in two steps, one with a T_{50} value of approximately 300 K, the other around 470 K. This suggests there are multiple Eu^{2+} sites present in the sample.
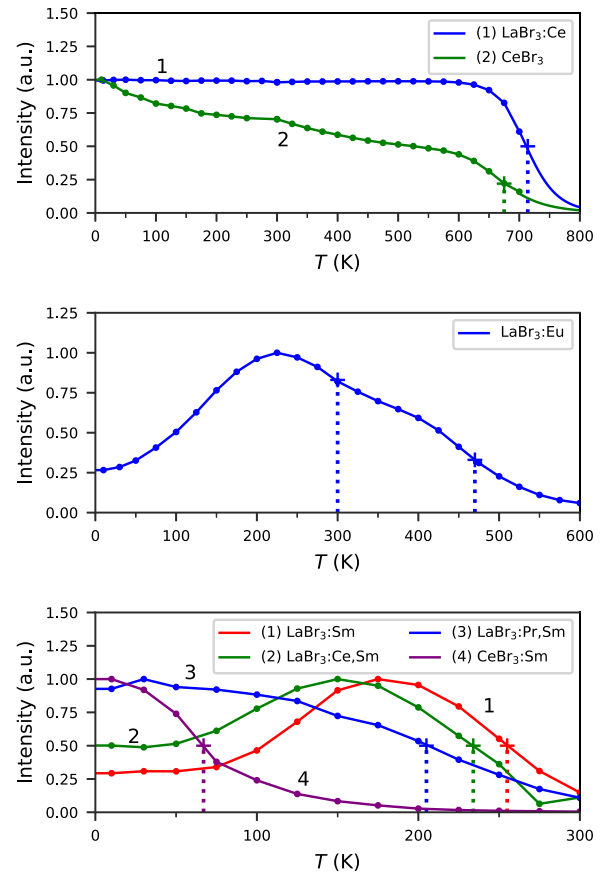
Fig. 4c shows the X-ray excited emission intensity of the four Sm^{2+}-doped samples. Just like LaBr$_3$:1%Eu^{2+}, the emission intensity of LaBr$_3$:1%Sm^{2+} (curve 1) becomes 4 times more intense upon increasing the temperature from 10 K to 200 K. Further increasing the temperature beyond 200 K causes thermal quenching and rapidly decreases the intensity. The emission intensity of LaBr$_3$:1%Sm^{2+} however does not drop in two steps, as was observed for LaBr$_3$:1%Eu^{2+}. T_{50} is reached at 255 K.

LaBr$_3$:5%Ce^{3+},1%Sm^{2+} (curve 2) shows similar behaviour to LaBr$_3$:1%Sm^{2+}. Increasing the temperature from 10 K initially causes the intensity to increase after which thermal quenching starts. The increase in intensity between 10 K and 150 K is however two times less than for LaBr$_3$:1%Sm^{2+}, which could be caused by Ce^{3+} competing with traps at capturing electrons from the conduction band. Another difference is that thermal quenching begins at approximately 25 K lower temperature compared to LaBr$_3$:1%Sm^{2+}, giving a T_{50} value of 235 K.

The intensity of LaBr$_3$:1%Pr^{3+},1%Sm^{2+} gradually decreases upon increase of the temperature from 10 K to 300 K. No clear onset of thermal quenching is observed. The total intensity reached 50% of its maximum value at 205 K. Lastly, the CeBr$_3$:Sm^{2+} emission intensity also exclusively decreases upon heating from 10 K. The quenching behaviour is not as gradual as in LaBr$_3$:1%Pr^{3+},1%Sm^{2+} and resembles that of the thermal quenching of LaBr$_3$:1%Sm^{2+}, but occurring at 185 K lower temperature, giving a T_{50} value of 70 K. The T_{50} values of all compounds are provided in Table 1.

For each compound, the light yield was determined at the temperature at which the X-ray excited emission spectrum has its highest intensity, and also at 300 K. Both light yield values are provided in Table 1. The sample with the lowest light yield of 7000 ph/MeV is

Table 1

Overview of maximum light yield $Y_{\max}$ determined at temperature $T_{\max}$, the light yield at 300 K Y_{300K} and quenching temperature T_{50} of LaBr$_3$-type samples with various dopants.

Sample	$Y_{\max}$ (ph/MeV)	$T_{\max}$ (K)	Y_{300K} (ph/MeV)	T_{50} (K)
LaBr$_3$:Ce^{3+}	76,000	10–600	76,000 [24]	715
CeBr$_3$	78,000	10	55,000 [25]	675
LaBr$_3$:1%Eu^{2+}	21,000	225	17,000	300, 470
LaBr$_3$:1%Sm^{2+}	7000	175	1000	255
LaBr$_3$:5%Ce^{3+}, 1 %Sm^{2+}	25,000	150	3000	235
LaBr$_3$:1%Pr^{3+}, 1%Sm^{2+}	17,000	10	2000	205
CeBr$_3$:1%Sm^{2+}	34,000	10	0	70

LaBr$_3$:Sm^{2+}, recorded at 175 K. Co-doping with 5% Ce^{3+} resulted in a significant increase to 25,000 ph/MeV, but the maximum intensity was attained at 150 K. For CeBr$_3$:1%Sm, a further increase to 34,000 ph/MeV is observed, but now at 10 K. This indicates the effectiveness of using Ce^{3+} as a scintillation sensitiser for Sm^{2+} in LaBr$_3$, but also shows its negative effect on the quenching temperature. At room temperature, thermal quenching causes the light yields of the Sm^{2+}-doped samples to be lower than their maximum value. However, even though LaBr$_3$:5%Ce^{3+},1%Sm^{2+} quenches at lower temperature than LaBr$_3$:1%Sm^{2+}, the room temperature light yield of the 5% Ce^{3+} co-doped sample is still higher than the sample without Ce^{3+} co-doping.

In both LaBr$_3$:Ce^{3+} and CeBr$_3$ that were co-doped with Ca^{2+}, Sr^{2+} or Ba^{2+}, the decrease in light yield when cooling below room temperature was observed together with shallow electron traps creating TL glow peaks between 50 K and 300 K [24,26]. The origin of these electron traps was suggested to be Br$^-$ vacancies forming as charge compensation for the divalent ions incorporated in the lattice. To investigate whether this is also the case for Eu^{2+} and Sm^{2+} samples, TL glow curves are shown in Fig. 5. Glow peaks are observed for LaBr$_3$:1%Eu^{2+}, LaBr$_3$:1%Sm^{2+} and LaBr$_3$:5%Ce^{3+},1%Sm^{2+} at temperatures where the light yield increases under X-ray excitation in Fig. 4c. No TL signal above noise level was found for LaBr$_3$:1%Pr^{3+},1%Sm^{2+} and CeBr$_3$:1%Sm^{2+}, which both show maximal intensity under X-ray excitation at 10 K.

A Br$^-$ vacancy sitting next to Eu^{2+} or Sm^{2+} would turn the regular 9 fold coordinated site into an 8 fold coordinated site and thereby remove the relaxation mechanism causing the unusually large Stokes shift. To study this, photoluminescence excitation and emission measurements were performed. Fig. 6a shows the photoluminescence emission and excitation spectra of LaBr$_3$:5%Ce^{3+}. The emission spectrum (curve 1) shows the Ce^{3+} 5d → 4f emission bands between 350 nm and 425 nm. The STE emission around 440 nm is not visible under photoexcitation at 295 nm. The excitation spectrum (curve 2) shows the 5 Ce^{3+} bands between 250 nm and 350 nm split up due to the crystal field splitting. The Stokes shift is determined to be 0.58 eV. The band between 210 nm and 250 nm is the host exciton band of LaBr$_3$ [6].

Fig. 6b shows the photoluminescence emission and excitation spectra of LaBr$_3$:1%Eu^{2+}. Under excitation at 300 nm, the emission spectrum (curve 1) shows only the Eu^{2+} 4f^{6}5d → 4f^7 emission band. The broad band emission around 600 nm observed under X-ray excitation in Fig. 2c is not visible here, showing that this emission does not originate from Eu^{2+}. The excitation spectrum (curve 2) features no clear structure. Based on the small bend in the excitation spectrum near 380 nm, the band corresponding to excitation into the Eu^{2+} 5d$_1$ level is approximated at 385 nm, giving a Stokes shift of 0.35 eV. This is in good agreement with the expectation that the Eu^{2+} Stokes shift is 0.61 times that of Ce^{3+} [27] and suggests that most of the Eu^{2+} emission comes from the same 9 fold coordinated sites that Ce^{3+} occupies in LaBr$_3$. The excitation spectrum of the Eu^{2+} emission shows a sudden drop in intensity at 230 nm where the host exciton band of LaBr$_3$ is located. This indicates that energy transfer from host excitons to Eu^{2+} is inefficient and is in line with the significantly lower value for the light yield compared to LaBr$_3$:Ce^{3+} given in Table 1.
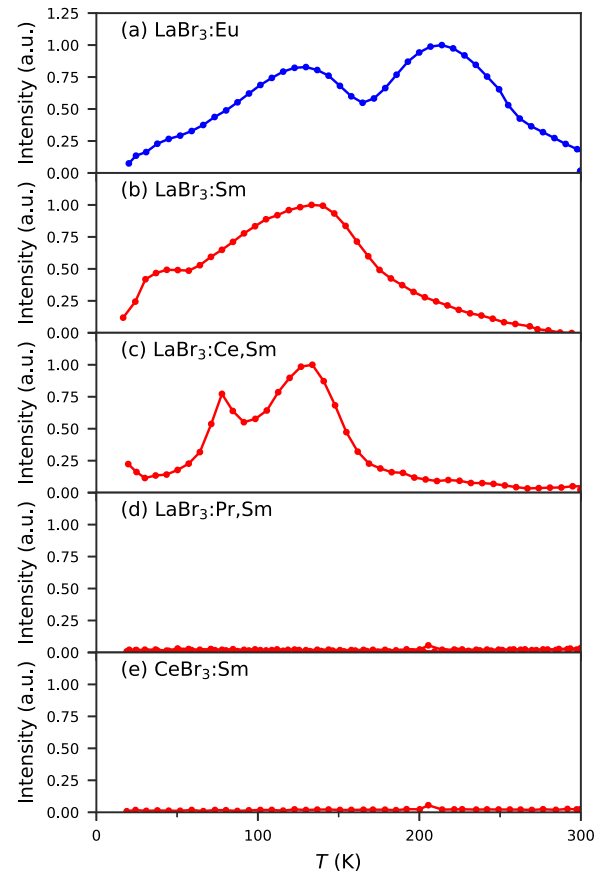
Fig. 5. Thermoluminescence glow curves with 15 K/min heating rate of (a) LaBr$_3$:1%Eu^{2+}, (b) LaBr$_3$:1%Sm^{2+}, (c) LaBr$_3$:5%Ce^{3+},1%Sm^{2+}, (d) LaBr$_3$:1%Pr^{3+},1%Sm^{2+} and (e) CeBr$_3$:1%Sm^{2+}.
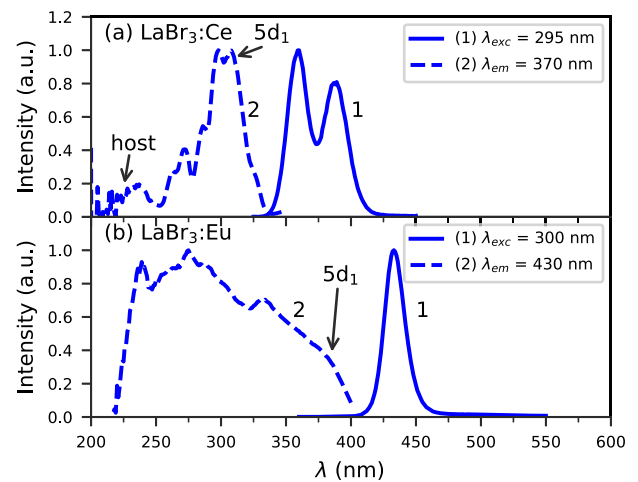
Fig. 6. Photoluminescence excitation and emission spectra at 10 K of (a) LaBr$_3$:5%Ce^{3+} and (b) LaBr$_3$:1%Eu^{2+}. No Eu^{2+} emission is observed when exciting the LaBr$_3$ host.

Fig. 7a shows the photoluminescence emission and excitation spectra of LaBr$_3$:1%Sm^{2+} at 10 K. Similar to under X-ray excitation in Fig. 3a, the emission spectrum (curve 1) shows exclusively Sm^{2+} 4f^6 → 4f^6 lines between 690 nm and 850 nm. The excitation spectrum (curve 2) shows that Sm^{2+} absorbs across the entire visible spectrum, but shows a sudden drop in intensity at 230 nm similar to what was
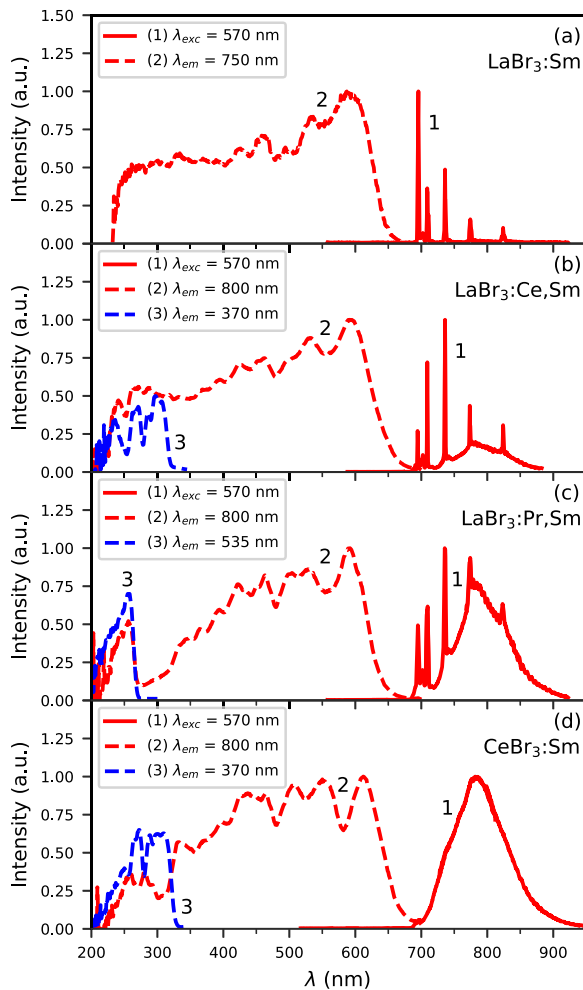
Fig. 7. Photoluminescence excitation and emission spectra at 10 K of (a) LaBr$_3$:1%Sm^{2+}, (b) LaBr$_3$:5%Ce^{3+},1%Sm^{2+}, (c) LaBr$_3$:1%Pr^{3+},1%Sm^{2+} and (d) CeBr$_3$:1%Sm^{2+}. The bands of Ce^{3+} and Pr^{3+} are visible in the excitation spectrum of Sm^{2+} in co-doped samples.

Fig. 8. Photoluminescence decay curves of LaBr$_3$:1%Sm^{2+} excited at 570 nm and observed at 800 nm, (a) between 10 K and 150 K, (b) between 10 K and 150 K on a shorter timescale, (c) between 150 K and 300 K.

observed for LaBr$_3$:1%Eu^{2+}. The low light yield given in Table 1 can therefore be explained by inefficient energy transfer from host excitons to Sm^{2+}.

In Fig. 7b, the photoluminescence emission and excitation spectra of LaBr$_3$:5%Ce^{3+},1%Sm^{2+} at 10 K are shown. The emission spectrum (curve 1) shows Sm^{2+} 4f^6 → 4f^6 lines on top of a weak 4f^{5}5d → 4f^6 band. This implies that the Sm^{2+} 5d$_1$ level is shifted to slightly lower energies as a result of Ce^{3+} co-doping. The excitation spectrum of the Sm^{2+} emission (curve 2) shows the structure of the Ce^{3+} excitation bands between 200 nm and 340 nm. For comparison, curve 3 shows the excitation spectrum of the Ce^{3+} emission in this sample. The excitation spectrum of the Sm^{2+} emission no longer shows a sudden drop at 230 nm. This indicates that host excitons can transfer their energy to Ce^{3+} which in turn can pass it on to Sm^{2+}. This is in line with the increase in light yield observed when co-doping LaBr$_3$:1%Sm^{2+} with Ce^{3+}, as shown in Table 1.

Fig. 7c shows the photoluminescence emission and excitation spectra of LaBr$_3$:1%Pr^{3+},1%Sm^{2+} at 10 K. The emission spectrum (curve 1) shows a further increase in the ratio of Sm^{2+} 4f^{5}5d → 4f^6 to 4f^6 → 4f^6 emission compared to the LaBr$_3$:5%Ce^{3+},1%Sm^{2+} sample. The excitation spectrum of the Sm^{2+} emission (curve 2) shows an intense band around 250 nm, which is also visible in the excitation spectrum of the Pr^{3+} emission (curve 3). This band is assigned to the Pr^{3+} CT band [6]. From this can be concluded that also Pr^{3+} serves as an intermediate step in energy transfer from host exciton to Sm^{2+}.

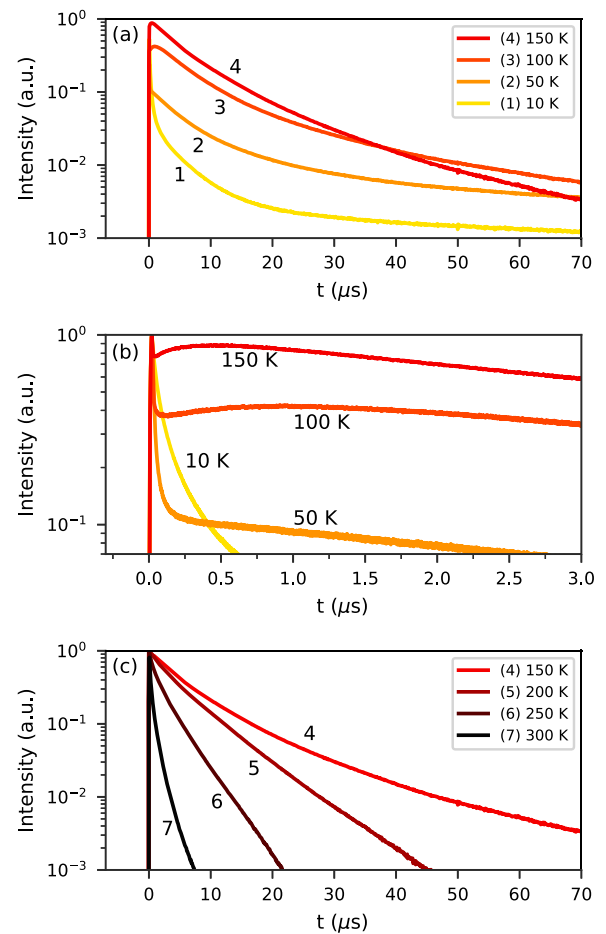Lastly, Fig. 7d shows the photoluminescence emission and excitation spectra of CeBr$_3$:1%Sm^{2+} at 10 K. Just like under X-ray excitation, exclusively Sm^{2+} 4f^{5}5d → 4f^6 emission is visible in the emission spectrum (curve 1), indicating that the Sm^{2+} 5d$_1$ level is further shifted to lower energies. The excitation spectrum of the Sm^{2+} emission (curve 2) shows an anti-correlation with the excitation spectrum of the Ce^{3+} emission (curve 3). This means that energy transfer is inefficient, which can be caused by saturation effects due to the high absorption strength of CeBr$_3$ combined with a low Sm^{2+} concentration.

The decay dynamics of Sm^{2+} can give insight in the presence of multiple sites and the decay time is also an important characteristic for application. Therefore, photoluminescence decay curves of LaBr$_3$:Sm^{2+} are shown in Fig. 8 upon excitation at 570 nm. Fig. 8a shows the decay curves between 10 K and 150 K. At 10 K (curve 1), the decay shows strong non-exponential behaviour containing an initial fast component with a decay time faster than 100 ns. Gradually, the decay slows down and a slow component of around 100 μs appears. Upon increasing the temperature to 150 K (curve 4), the fast component gradually disappears and the slow component becomes faster.

On a timescale of the first few μs after excitation, the temperature dependent behaviour is more complex. For this, a zoom in of the first 3 μs of the decay curves shown in Fig. 8a is shown in Fig. 8b. Here it becomes visible that upon increasing the temperature from 10 K to 50 K, the fast component becomes even faster and a plateau develops in the luminescence decay curve between 0.2 μs and 1 μs. Upon increasing the temperature further to 100 K and 150 K, this plateau develops into a build up of the signal, indicating the 4f^{5}5d
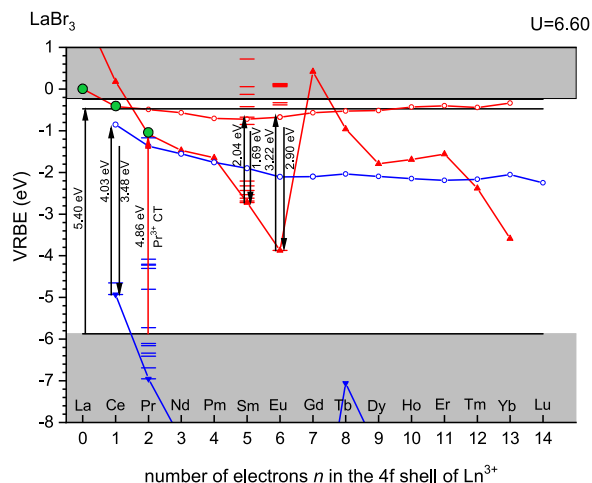
Fig. 9. VRBE diagram of lanthanide levels in LaBr$_3$, for details see the text in Discussion. The 5d$_1$ levels of Eu^{2+} and Sm^{2+} are located closer to the conduction band bottom than that of Ce^{3+}, explaining the lower quenching temperatures.

Fig. 10. VRBE diagram for Ce^{3+} and Sm^{2+} in LaBr$_3$, CeBr$_3$, and PrBr$_3$. The lowering of the conduction band bottom along the series decreases the quenching temperature of Ce^{3+} and Sm^{2+} 4f^{n-1}5d $\rightarrow$ 4f^n emissions.

Table 2
Parameters used for constructing the VRBE diagram in Fig. 10. All values are given in units of eV.

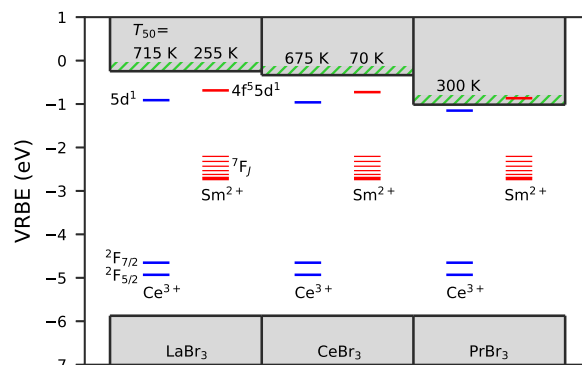| Host	U	E_G	E_{CT}^{Eu3+}	E_{5d}^{Ce3+}	E_{5d}^{Sm2+}
LaBr$_3$	6.60 [30]	5.63	2.09 [30]	4.02	2.04
CeBr$_3$	6.60 [30]	5.54	2.09 [30]	3.97	2.00
PrBr$_3$	6.60 [30]	4.86	2.09 [30]	3.78 [31]	1.86

level becomes more populated, likely from crossover from the 4f^6[$^5D_0$] level. The fast component however still persists while this build up with slower time constant develops. This behaviour can only be explained with multiple Sm^{2+} sites being present in the sample, some of which create the fast component and others cause the build up in signal.

The decay curves in Fig. 8c are collected at temperatures between 150 K and 300 K, which is the temperature range in which thermal quenching of the X-ray excited emission takes place (Fig. 4c). Going from 150 K (curve 4) to 200 K (curve 5), the strong non-exponential behaviour disappears, coinciding with the disappearing of the 4f$^6 \rightarrow$ 4f^6 lines in the X-ray excited emission spectrum in Fig. 3a. However, the decay curves are still not well described by single exponential functions, again hinting towards the presence of multiple sites. Increasing the temperature further above 200 K causes the decay time to rapidly become shorter, which confirms that this is the temperature range in which thermal quenching takes place.

4. Discussion

Incorporating divalent ions such as Sm^{2+} in a LaBr$_3$ lattice requires charge compensation, as was previously discussed by Alekhin et al. [24,28]. It was found that co-doping LaBr$_3$:Ce^{3+} with Ca^{2+}, Sr^{2+}, or Ba^{2+} creates two additional Ce^{3+} sites, creates electron traps that cause TL peaks between 78 K and 300 K, and decreases the light yield below room temperature. The suggested charge compensation mechanism was the creation of Br$^-$ vacancies. The decrease in light yield below room temperature (Fig. 4a and b) and accompanying TL peaks (Fig. 5) were also observed for LaBr$_3$:1%Eu^{2+}, LaBr$_3$:1%Sm^{2+}, and LaBr$_3$:5%Ce^{3+},1%Sm^{2+}. As Eu^{2+} and Sm^{2+} have the same charge and a similar ionic radius as Sr^{2+}, the same mechanism of charge compensation in the form of Br$^-$ vacancies can be expected here.

Intuitively, Br$^-$ vacancies would locate right next to the divalent dopant ion. Along the series LaBr$_3$, CeBr$_3$, PrBr$_3$, NdBr$_3$, the rare earth ion radius decreases. As a result, the crystal structure of the MBr$_3$ bromide changes from the UCl$_3$ structure for M = La - Pr to the PuBr$_3$ structure for M = Nd and the coordination number of the rare earth ion is reduced from nine to eight, respectively. As Eu^{2+} and Sm^{2+} have larger ionic radii than La^{3+}, they prefer a higher coordination number and occupy the regular cation site with 9-fold coordination, rather than the neighbourhood of a Br$^-$ vacancy with a reduced coordination number of eight. The analysis of the Stokes shift of Eu^{2+} suggests that most of the emission comes from the 9 fold coordinated site, even

though the photoluminescence decay of Sm^{2+} showed that multiple sites are still present in the LaBr$_3$:1%Sm^{2+} sample.

To rationalise the quenching mechanism of Sm^{2+} in LaBr$_3$, a vacuum referred binding energy (VRBE) diagram has been constructed, which is shown in Fig. 9. The parameters used for constructing the diagram are summarised in Table 2. The band gap E_G of LaBr$_3$ is estimated from the exciton band according to Ref. [29]. The 4f$^n \rightarrow$ 4f^{n-1}5d transition energies of Ce^{3+} and Sm^{2+} (E_{5d}^{Ce3+} and E_{5d}^{Sm2+}) are based on spectroscopic data presented in this work and extrapolated to other lanthanides using Refs. [15,16]. The triangles connected by the zigzag curves indicate the lowest 4f^n states of trivalent (blue) and divalent (red) lanthanides. The dots indicate their respective 5d$_1$ states. The excited 4f^n states of Ce^{3+}, Pr^{3+}, Sm^{2+} and Eu^{2+} are shown by horizontal lines. The arrows indicate transitions observed spectroscopically in this work. The resulting diagram shows that the 4f^{n-1}5d levels of Eu^{2+} and Sm^{2+} lie well above that of Ce^{3+} and thereby closer to the conduction band, while also the T_{50} of Eu^{2+} and Sm^{2+} is much lower than that of Ce^{3+} (Fig. 4). This suggests that thermal quenching takes place via 5d electron ionisation to the conduction band.

In PrBr$_3$, the T_{50} of the Ce^{3+} emission is 300 K. Birowosuto et al. suggested that quenching of Ce^{3+} emission in PrBr$_3$:Ce^{3+} happens through charge transfer from the 5d excited state of Ce^{3+} to the Pr^{2+} ground state [31]. The ground state of Pr^{2+} is the 4f^3 ground state, which lies well below the conduction band minimum in LaBr$_3$. Creating Pr^{2+} in PrBr$_3$ is analogous to placing an electron at the bottom of the conduction band, which implies that the conduction band minimum of PrBr$_3$ lies at approximately 1 eV lower energy compared to that of LaBr$_3$. Assuming the valence band maximum at the same energy in LaBr$_3$ and PrBr$_3$, the conduction band minimum of PrBr$_3$ can be estimated using the Pr^{3+} CT band in LaBr$_3$. From this reasoning follows that quenching of Ce^{3+} emission in PrBr$_3$ also occurs via 5d electron ionisation to the conduction band.

To illustrate the change in conduction band minimum and its relation to T_{50}, Fig. 10 has been constructed where the Ce^{3+} and Sm^{2+} energy levels are shown in the band gap of LaBr$_3$, CeBr$_3$ and PrBr$_3$ together with the T_{50} values of the Ce^{3+} and Sm^{2+} emission. It is assumed that the U parameter and CT transition energy of Eu^{3+} (E_{CT}^{Eu3+}) and consequently the valence band maximum are constant between the compounds. The values of E_{5d}^{Ce3+} and E_{5d}^{Sm2+} are adjusted to spectroscopic data, only E_{5d}^{Sm2+} in PrBr$_3$ is estimated based on the redshift of
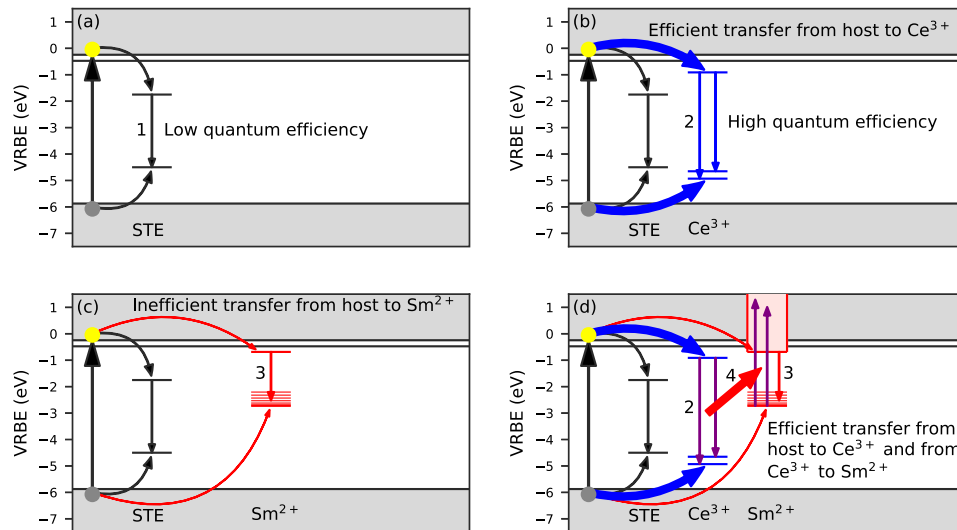
Fig. 11. Diagram showing the scintillation sensitising mechanism of Ce^{3+}. (a) Undoped $LaBr_3$ shows low quantum efficiency STE emission, (b) doping with Ce^{3+} introduces an efficient route of energy transfer from host to Ce^{3+} and creates stable emission at room temperature, (c) energy transfer from host to Sm^{2+} is inefficient and (d) efficient transfer from host to Ce^{3+} and subsequent energy transfer from Ce^{3+} to Sm^{2+} creates an efficient route of energy transfer from host to Sm^{2+}.

the Ce^{3+} 5d level. The conduction band minimum of $CeBr_3$ is estimated from the change in quenching temperature (ΔT_{50}) of the Ce^{3+} emission compared to that in $LaBr_3$ and $PrBr_3$ through Eq. (1) [32]:

$$\Delta T_{50} = \frac{11600}{\ln(\tau_v \Gamma_0)} \Delta E \qquad (1)$$

Here, τ_v is radiative lifetime of Ce^{3+} and Γ_0 is approximately the highest phonon frequency in $LaBr_3$. The used values for τ_v and Γ_0 is are 30 ns [1] and 5×10^{12} Hz [33], respectively. ΔE is the energy gap between the Ce^{3+} 5d level and the conduction band bottom. All parameters required to construct Fig. 10 are also summarised in Table 2.

Fig. 10 shows that the conduction band minimum decreases in energy when changing the host cation from La^{3+} to Ce^{3+} to Pr^{3+}, while simultaneously T_{50} decreases. The energy of the conduction band minimum follows the same trend as that of the ground state energy of La^{2+}, Ce^{2+}, and Pr^{2+} marked with green circles in the VRBE diagram in Fig. 9. This also explains why T_{50} of the Sm^{2+} emission decreases upon co-doping $LaBr_3:1\%Sm^{2+}$ with Ce^{3+}, as upon co-doping with Ce^{3+} a gradual decrease in conduction band energy is expected. In the case of $LaBr_3:1\%Pr^{3+},1\%Sm^{2+}$ the quenching of Sm^{2+} emission is a gradual process and no distinct quenching temperature was observed. This is likely caused by the low Pr^{3+} concentration. The quenching temperature of a Sm^{2+} ion then depends on the distance to the nearest Pr^{3+} ion, giving a large distribution of quenching temperatures. As the Sm^{2+} $4f^5 5d$ level lies close to the Pr^{2+} $4f^3$ ground state, the quenching is indeed expected to start from temperatures as low as 10 K. Sm^{2+} would then likely not show any emission at all in $PrBr_3$ due to the $4f^5 5d$ state lying in the conduction band.

Despite reducing the quenching temperature of Sm^{2+}, co-doping $LaBr_3:Sm^{2+}$ with Ce^{3+} or Pr^{3+} as scintillation sensitiser drastically increases its light yield, as can be seen in Table 1. Pr^{3+} does not transfer its energy efficiently to Sm^{2+}, as still a lot of Pr^{3+} emission is present in Fig. 3c. However, the intensity of the Ce^{3+} emission is low in Fig. 3b and d, indicating that Ce^{3+} is a suitable sensitiser.

The mechanism of sensitisation is portrayed in Fig. 11. Fig. 11a shows the case of undoped $LaBr_3$, where most of the emission is STE emission, indicated by arrow 1. The STE emission energy is drawn accurately, but the position of the energy levels within the band gap is chosen arbitrarily. Below 150 K, the light yield of undoped $LaBr_3$ is the same as that of $LaBr_3:Ce^{3+}$, but the emission is thermally quenched

with a T_{50} of 225 K [34]. Doping $LaBr_3$ with Ce^{3+} creates the situation of Fig. 11b. The transfer of electrons and holes to Ce^{3+} competes with STE formation and almost all emission comes from Ce^{3+} with doping concentrations of a few percent, indicated by arrows 2.

When doping $LaBr_3$ with 1% Sm^{2+}, the situation of Fig. 11c is created. Sm^{2+} emission is visible, as indicated by arrow 3, but the light yield has drastically dropped to only 7000 ph/MeV at its maximum at 175 K. Additionally, the intensity of the excitation spectrum of Sm^{2+} emission in $LaBr_3:1\%Sm^{2+}$ drops to zero upon exciting the $LaBr_3$ host below 230 nm (Fig. 7a). These two observations indicate that energy transfer from the host to Sm^{2+} is inefficient.

When co-doping $LaBr_3:1\%Sm^{2+}$ with 5% Ce^{3+} (Fig. 11d), electrons and holes can again be efficiently transferred to Ce^{3+}. This is confirmed by the remaining Ce^{3+} emission in the X-ray excited spectra in Fig. 3b, displaying that Ce^{3+} gets excited during the scintillation process. As the $5d \rightarrow 4f$ emission bands of Ce^{3+} overlap with the $4f^6 \rightarrow 4f^5 5d$ excitation bands of Sm^{2+}, most of the Ce^{3+} excitations are transferred to Sm^{2+} through radiationless energy transfer, indicated by arrow 4. In this way, the efficient transfer from host to Ce^{3+} is used to sensitise Sm^{2+} and the light yield increases from 7000 ph/MeV for $LaBr_3:1\%Sm^{2+}$ to 25,000 ph/MeV for $LaBr_3:5\%Ce^{3+},1\%Sm^{2.+}$. The same inefficient transfer from host to lanthanide is also seen in $LaBr_3:1\%Eu^{2+}$ and it can therefore be expected that co-doping with Ce^{3+} improves its light yield as well.

5. Conclusions

The possibility of using Sm^{2+} as an activator for $LaBr_3$ has been investigated. The Sm^{2+} emission wavelength is found to be in the optimal range for readout with silicon based photodetectors. However, energy transfer from the $LaBr_3$ host to both Eu^{2+} and Sm^{2+} is inefficient, but can be greatly improved by using Ce^{3+} as a scintillation sensitiser. The light yield of $LaBr_3:1\%Sm^{2+}$ improved from 7000 ph/MeV to 25,000 ph/MeV upon co-doping with 5% Ce^{3+}. Host excitations are efficiently transferred to Ce^{3+}, which in turn transfers its excitations to Sm^{2+}. Energy transfer from Pr^{3+} to Sm^{2+} was shown to be inefficient. The downside of using Ce^{3+} or Pr^{3+} as a co-dopant is that it decreases the quenching temperature of Sm^{2+}. All Sm^{2+}-doped samples experienced thermal quenching already below room temperature. Doping $LaBr_3$ with Eu^{2+} and Sm^{2+} creates charge compensating defects similar to what is seen upon Sr^{2+} co-doping. These defects act as electron traps and reduce the light output below room temperature.

CRediT authorship contribution statement

Casper van Aarle: Conceptualization, Investigation, Writing – original draft, Visualization. **Nils Roturier:** Conceptualization, Investigation, Writing – original draft, Visualization. **Daniel A. Biner:** Resources. **Karl W. Krämer:** Resources, Writing – review & editing. **Pieter Dorenbos:** Writing – review & editing, Funding acquisition.

Declaration of competing interest

The authors declare that they have no known competing financial interests or personal relationships that could have appeared to influence the work reported in this paper.

Data availability

Data will be made available on request.

Acknowledgement

References

[1] E.V.D. van Loef, P. Dorenbos, C.W.E. van Eijk, K. Krämer, H.U. Güdel, Appl. Phys. Lett. 79 (2001) 1573.
[2] M.E. Daube-Witherspoon, S. Surti, A. Perkins, C.C.M. Kyba, R. Wiener, M.E. Werner, R. Kulp, J.S. Karp, Phys. Med. Biol. 55 (2010) 45.
[3] Stefan J. van der Sar, David Leibold, Stefan E. Brunner, Dennis R. Schaart, Proc. SPIE 12304 (2022) 123040A.
[4] A. Kozyrev, I. Mitrofanov, A. Owens, F. Quarati, J. Benkhoff, B. Bakhtin, F. Fedosov, D. Golovin, M. Litvak, A. Malakhov, M. Mokrousov, I. Nuzhdin, A. Sanin, V. Tretyakov, A. Vostrukhin, G. Timoshenko, V. Shvetsov, C. Granja, T. Slavicek, S. Pospisil, Rev. Sci. Intrum. 87 (2016) 085112.
[5] B.D. Milbrath, B.J. Choate, J.E. Fast, W.K. Hensley, R.T. Kouzes, J.E. Schweppe, Nucl. Instrum. Methods A 572 (2007) 774.
[6] P. Dorenbos, E.V.D. van Loef, A.P. Vink, E. van der Kolk, C.W.E. van Eijk, K.W. Krämer, H.U. Güdel, W.M. Higgins, K.S. Shah, J. Lumin. 117 (2006) 147.
[7] David N. ter Weele, Dennis R. Schaart, Pieter Dorenbos, IEEE Trans. Nucl. Sci. 61 (2014) 683.
[8] F.G.A. Quarati, P. Dorenbos, J. van der Biezen, Alan Owens, M. Selle, L. Parthier, P. Schotanus, Nucl. Instrum. Methods A 729 (2013) 596.
[9] J. Andriessen, E. van der Kolk, P. Dorenbos, Phys. Rev. B 76 (2007) 075124.
[10] W.H. Zachariasen, Acta Crystallogr. 1 (1948) 265.
[11] M.S. Alekhin, J.T.M. de Haas, I.V. Khodyuk, K.W. Krämer, P.R. Menge, V. Ouspenski, P. Dorenbos, Appl. Phys. Lett. 102 (2013) 151915.
[12] Johan T.M. de Haas, Pieter Dorenbos, IEEE Trans. Nucl. Sci. 55 (2008) 1086.
[13] J. Glodo, R. Farrell, E.V.D. van Loef, W.M. Higgins, K.S. Shah, IEEE Nucl. Sci. Conf. R. (2005) 98.
[14] Daniel Rutstrom, Robyn Collette, Luis Stand, Matthew Loyd, Yuntao Wu, Merry Koschan, Charles L. Melcher, Mariya Zhuravleva, J. Cryst. Growth 483 (2018) 251.
[15] P. Dorenbos, J. Lumin. 91 (2000) 155.
[16] P. Dorenbos, J. Phys. Condens. Mat. 15 (2003) 575.
[17] Laura C. Dixie, Andrew Edgar, Murray C. Bartle, J. Lumin. 149 (2014) 91.
[18] R.H.P. Awater, M.S. Alekhin, D.A. Biner, K.W. Krämer, P. Dorenbos, J. Lumin. 212 (2019) 1.
[19] Daisuke Nakauchi, Yutaka Fujimoto, Takumi Kato, Noriaki Kawaguchi, Takayuki Yanagida, Crystals 12 (2022) 517.
[20] Casper van Aarle, Karl W. Krämer, Pieter Dorenbos, J. Mater. Chem. C 11 (2023) 2336.
[21] D.L. Dexter, J. Chem. Phys. 21 (1953) 836.
[22] Weronika Wolszczak, Karl W. Krämer, Pieter Dorenbos, Phys. Status Solidi R 13 (2019) 1900158.
[23] G. Meyer, Advances in the Synthesis and Reactivity of Solids, Vol. 2, JAI Press Inc, 1994, pp. 1–16.
[24] Mikhail S. Alekhin, Daniel A. Biner, Karl W. Krämer, Pieter Dorenbos, J. Appl. Phys. 113 (2013) 224904.
[25] F.G.A. Quarati, M.S. Alekhin, K.W. Krämer, P. Dorenbos, Nucl. Instrum. Methods A 735 (2014) 655.
[26] Roy H.P. Awater, Karl W. Krämer, P. Dorenbos, IEEE Trans. Nucl. Sci. 62 (2015) 2343.
[27] P. Dorenbos, J. Phys. Condens. Matter 15 (2003) 4797.
[28] Mikhail S. Alekhin, Sandra Weber, Karl W. Krämer, Pieter Dorenbos, J. Lumin. 145 (2014) 518.
[29] P. Dorenbos, J. Lumin. 111 (2005) 89.
[30] Pieter Dorenbos, Aday Josef, Johan T.M. de Haas, Karl W. Krämer, J. Lumin. 208 (2019) 463.
[31] M.D. Birowosuto, P. Dorenbos, C.W.E. van Eijk, K.W. Krämer, H.U. Güdel, J. Phys. Condens. Matter. 19 (2007) 256209.
[32] Pieter Dorenbos, J. Mater. Chem. C (2023) Advance Article.
[33] Isaac Richman, Robert A. Satten, Eugene Y. Wong, J. Chem. Phys. 39 (1963) 1833.
[34] E.V.D. van Loef, P. Dorenbos, C.W.E. van Eijk, K.W. Krämer, H.U. Güdel, Nucl. Instrum. Methods A 486 (2002) 254.